CrossMark

ORIGINAL PAPER

A hybrid approach for modeling of breakable granular materials using combined finite-discrete element method

Gang Ma[1] · **Wei Zhou**[1] · **Xiao-Lin Chang**[1] · **Ming-Xiang Chen**[1]

Abstract It is well known that particle breakage plays a critical role in the mechanical behavior of granular materials and has been a topic subject to intensive studies. This paper presents a three dimensional fracture model in the context of combined finite-discrete element method (FDEM) to simulate the breakage of irregular shaped granular materials, e.g., sands, gravels, and rockfills. In this method, each particle is discretized into a finite element mesh. The potential fracture paths are represented by pre-inserted non-thickness cohesive interface elements with a progressive damage model. The Mohr–Coulomb model with tension cut-off is employed as the damage initiation criterion to rupture the predominant failure mode at the particle scale. The particle breakage modeling using combined FDEM is validated by the qualitative agreement between the results of simulated single particle crushing tests and those obtained from laboratory tests and prior DEM simulations. A comprehensive numerical triaxial tests are carried out on both the unbreakable and breakable particle assemblies with varied confining pressure and particle crushability. The simulated stress–strain–dilation responses of breakable granular assembly are qualitatively in good agreement with the experimental observations. The effects of particle breakage on the compressibility, shear strength, volumetric response of the fairly dense breakable granular assembly are thoroughly investigated through a variety of mechanism demonstrations and micromechanical

analysis. This paper also reports the energy input and dissipation behavior and its relation to the mechanical response.

1 Introduction

Particle breakage plays an important role in the mechanical behavior of granular materials, typically in high rockfill dams, where the contact forces acting on grains can be high enough to cause excessive particle crushing. In recognition of its importance in many geotechnical engineering applications, particle behavior has been a topic subject to intensive experimental studies over the past few decades [1–4]. The experimental studies have proved that particle breakage is related to many fundamental aspects of granular materials, such as dilatancy, strain hardening, shear band formation, energy dissipation, and creep deformation. However, all of the micromechanics related to the particle breakage are still not fully understood. This deficiency hinders the development of constitutive models incorporating the particle breakage effects.

In parallel with experimental studies, another major contribution in this field comes from the discrete element modeling pioneered by Robertson and Bolton [5] and later developed by Cheng et al. [6]. The theoretical basis of this work is that grains are taken to fracture probabilistically, the likelihood increasing with applied stress and can be described by Weibull's statistical distribution. On this basis, a wealth of numerical modeling works have been carried out to investigate the effects of particle breakage on the mechanical behavior of granular materials and its microscopic mechanism [7–11]. Previous works handing particle breakage are

✉ Wei Zhou
zw_mxx@163.com

Gang Ma
magang630@163.com

1 State Key Laboratory of Water Resources and Hydropower Engineering Science, Wuhan University, Wuhan 430072, China

mainly realized by the breakage of subparticles joined by bonding or cohesive forces. Another approach is to replace the particle fulfilling a predefined failure criterion with an equivalent group of smaller particles [12,13]. The recent development in this modeling approach includes the work done by de Bono and McDowell [14] and subsequently improved by Zhou et al. [15].

DEM has demonstrated its ability in reproducing the macroscopic response and exploring the microscopic mechanism of granular materials. However, problems still encountered with these DEM applications that reduce the physical behavior they attempt to model, namely deformability, fracture and shape representation, have long been recognized. The simplification of particle shapes will arise some computational issues when breakage occurs, such as the unrealistic release of voids initially enclosed by subparticles. For obeying conservation of mass, the total volume of new spheres is equal to that of the original parent sphere, this will produce local pressure spikes during breakage [14].

As observed by many researchers, the original boundary between continuous and discontinuous modeling techniques has become less clear as several techniques are capable of dealing with both the continuous and discontinuous problems. In particular, the hybrid approach known as the combined finite-discrete element method, which was first pioneered by Munjiza and Owen in 1990's [16], and later becoming established with a text book [17]. Hereinafter the combined finite-discrete element method is referred to as the combined FDEM. In discrete modeling of granular materials, the most attractive benefit of using combined FDEM is that various particle shapes can be easily introduced with a general contact solution. Latham and Munjiza simulated the gravitational deposition of irregular shaped units using combined FDEM, the comparison between simulated and experimental results demonstrates that combined FDEM can handle the interactions between complex-shaped particles with reasonable accuracy [18]. At present, the combined FDEM has been used in various scientific researches and engineering applications, such as rock engineering [19–22], granular materials [23,24], and coastal engineering [25,26].

However, in this context, while considerable advances have been made in the numerical construction of realistic granular materials [23,27], the modeling of fracture and fragmentation of granular materials has presented a considerable challenge which need us to develop a robust three dimensional fracture model in combined FDEM [24,26]. The research object of this paper is to develop a robust three dimensional fracture model within the framework of combined FDEM, and then use it to investigate the mechanical behavior of breakable granular materials as well as the energy transformation and dissipation behavior. First, the fundamental issues of combined FDEM, especially the three dimensional fracture model, are described in Sect. 2. Next is Sect. 3, single particle crushing tests are simulated and the results are compared with previous studies as a means of validating the particle breakage modeling using combined FDEM. In Sects. 4 and 5, a series of numerical triaxial tests are performed on a dense packing of irregular shaped particle assembly. The macroscopic behaviors of breakable granular materials are fully examined. This paper takes a further step to explore the energy transformation and dissipation during the shearing process, which offers deeper insights into the role of particle breakage in the mechanical behavior of granular materials. The most significant contribution of this paper is that we developed a practical and robust particle breakage modeling technique in the context of combined FDEM, which has the potential to capture the complex physical behavior of breakable granular materials.

2 Fundamental principles of combined FDEM

Combined FDEM incorporates aspects of both the finite element method and discrete element method into a uniform framework. By discretizing the discrete bodies into finite elements, the particle shape and deformability can be well described by FEM formulation, while the fracture and fragmentation, contact detection, interaction between separate bodies can be handled by DEM formulation. This hybrid approach can also be considered as full FEM, only the contact detection and interaction is "borrowed" from DEM. Compared with DEM, the hybrid approach is more versatile in dealing with deformable, irregular shaped and breakable discrete bodies. Compared with FEM, the hybrid approach is more robust and efficient in dealing with solid fracture and multi body collisions.

A typical combined FDEM simulation comprises a large number of interacting bodies. The main processes included in the combined FDEM are contact detection, contact interaction, finite strain elasticity as well as fracture and fragmentation. Each of those processes, but deformability, is briefly illustrated in the coming sections. Deformability is implemented as in any standard explicit finite element analysis and thus is not discussed any further here. In this study, the combined FDEM modeling of breakable granular materials are performed using the explicit module of the general-purposed finite element software ABAQUS/Explicit [28]. The explicit integration scheme and general contact capability of this module makes it appropriate for large number of actual and potential contacts undergoing large deformation.

2.1 Contact detection and interaction

Contact detection works in a similar way as in DEM modeling, which detects all the couples that are in contact and

eliminate couples that are too far and cannot possibly in contact. Once couples of discrete objects in contact have been detected, a contact interaction algorithm is used to evaluate contact forces between contacting bodies. The contact interaction algorithm takes advantage of the finite element discretization of discrete bodies, and combines this with the potential function method. The potential function method is based on the assumption that contacting couples tend to penetrate into each other generating distributed contact forces. This will yield realistic distribution of contact force over finite contact domain resulting from the overlap of contacting bodies. If the potentials are chosen to be constant on the boundaries of both contactor and target bodies, energy balance is preserved independent of the value of penalty term, shape and size of the overlap between two contacting bodies [17]. As penalty term tends to infinity, a body impenetrability condition is approached. Then a Coulomb-type friction law is implemented in the interaction algorithm based on the sliding distance of two contacting bodies.

2.2 Governing equations

In the combined FDEM modeling of granular materials, each particle is discretized by tetrahedral elements and cohesive elements without thickness that will be described in the next section. The motions of element nodes are governed by internal forces and external forces acting on them. The nodal forces include the contribution from contact interaction, deformation of a discrete element, and external loads, etc.. In general, the governing equations can be expressed as:

$$\mathbf{M}\frac{\partial^2 \mathbf{x}}{\partial t^2} + \mathbf{F}_{\text{int}} - \mathbf{F}_{\text{ext}} - \mathbf{F}_{\text{c}} = 0 \tag{1}$$

where $\mathbf{M}$ is the lumped mass matrix of the system, $\mathbf{x}$ is the vector of nodal displacements. $\mathbf{F}_{\text{int}}$, $\mathbf{F}_{\text{ext}}$ and $\mathbf{F}_{\text{c}}$ are the vectors of internal resisting forces, of applied external loads and of contact forces, respectively. Contact forces, $\mathbf{F}_{\text{c}}$ are calculated either between contacting bodies or along internal discontinuities, i.e., pre-existing and newly created fractures.
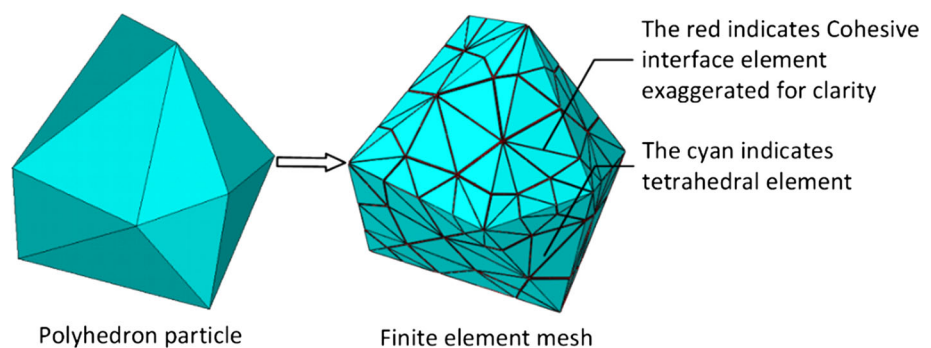
Internal resisting forces, $\mathbf{F}_{\text{int}}$, include the contribution from the elastic forces, $\mathbf{F}_{\text{e}}$, and the cohesive element bonding forces, $\mathbf{F}_{\text{coh}}$. The elastic forces, $\mathbf{F}_{\text{e}}$, are computed on an element-by-element basis under the assumption of isotropic linear elasticity. Cohesive element bonding forces, $\mathbf{F}_{\text{coh}}$, are used to simulate material failure, as further explained in the next section.

The equations of motion of element nodes are integrated using the explicit central-difference integration scheme. After the calculation of all the parts contributing to the nodal force in Eq. (1), the accelerations at the beginning of the increment are computed, and then the velocity and position at nodes are updated. The choice of time-step is important for the numerical stability of combined FDEM simulation, because the central-difference operator is conditionally stable. Both the FEM and DEM stability requirements should be satisfied simultaneously, so the ultimate time-step Δt used in the combined FDEM simulation is the smaller value between Δt_{FEM} and Δt_{DEM} [26].

2.3 Material failure model

The fracture and fragmentation is modelled using the cohesive zone model (CZM), which represents the mechanical processes in the fracture process zone (FPZ) ahead of the crack tip. Following an approach similar to that pioneered by Xu and Needleman [29], non-thickness cohesive interface elements (CIEs) are embedded between the edges of all adjacent tetrahedral element pairs from the very beginning of the simulation, as depicted in Fig. 1. Thus, the fracture of the material progresses solely on the damage and failure of cohesive elements while the bulk elements are treated as linear elastic using tetrahedral elements. Since fractures can nucleate and propagate only along the cohesive elements, the potential crack paths do not need to be assumed in advance and arbitrary fracture trajectories can be reproduced within the constraints imposed by the initial mesh topology. Unlike other fracture modeling techniques, remeshing is not performed and mesh topology is never updated during the simulation, so a relatively small element size should

Fig. 1 Discretization of irregular shaped particle into finite element mesh

Polyhedron particle

Finite element mesh

The red indicates Cohesive interface element exaggerated for clarity

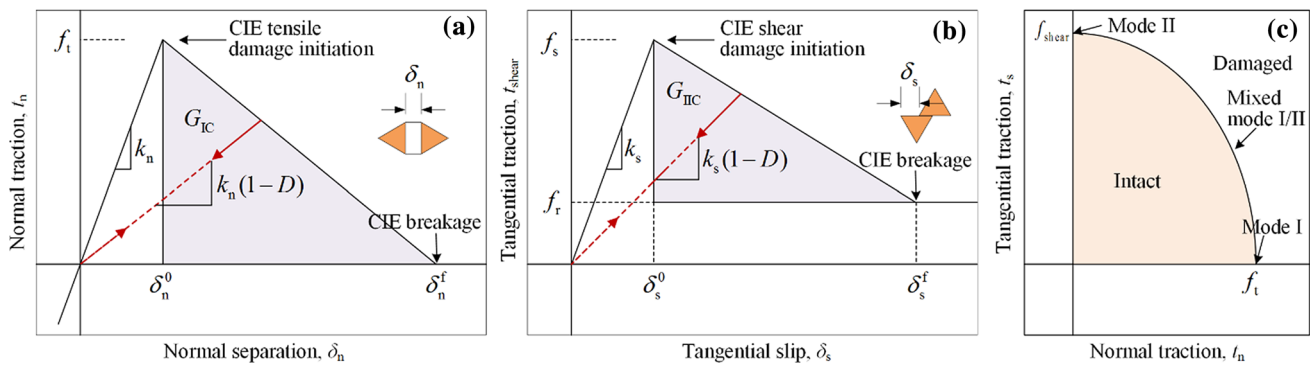The cyan indicates tetrahedral element

Fig. 2 Constitutive relations of cohesive interface elements

be adopted to reproduce the realistic fracture path. Upon breakage of the cohesive surface, the cohesive element is removed from the simulation and therefore the model locally transits from a continuum to a discontinuum. The newly created discontinuity is automatically recognized and modeled by the contact interaction. Compared with alternative analysis techniques, CZM offers the advantages of encompassing both crack initiation and crack propagation and the ability to model multiple crack paths, without the need for computationally expensive crack-path following algorithms. In addition, it does not require the direction of crack propagation to be known in advance, and cracks have the potential to propagate along any path where cohesive interface elements are placed.

There are three key ingredients in formulating the CZM, namely, damage initiation criterion, constitutive law, and critical energy release rate, G_C (as shown in Fig. 2). The relationship between relative displacement and traction inside the FPZ is characterized by the cohesive constitutive law, in which the traction and separation response is expressed in several functional forms, such as a trapezoidal function, a polynomial function, an exponential function, or most commonly a bilinear function [30]. Several investigations dealt with the effect of the shape of the traction-separation function on the simulated fracture behavior, and they came to the conclusion that the detailed shape of traction-separation curve is less important than the values of fracture energy and cohesive strength [31]. Thus a bilinear form of CZM is used due to its simplicity without losing the simulation accuracy.

For a 3D case, the nominal traction stress vector, $\mathbf{t}$, consists of three components: t_n, t_{s1}, and t_{s2} which represents the normal and two shear tractions, repressively. The corresponding relative displacements are denoted by δ_n, δ_{s1}, and δ_{s2}. The constitutive law in local coordinate system relates the interface tractions to the relative displacements as follows:

$$\mathbf{t} = \begin{Bmatrix} t_n \\ t_{s1} \\ t_{s2} \end{Bmatrix} = \begin{bmatrix} k_n & & \\ & k_s & \\ & & k_s \end{bmatrix} \begin{Bmatrix} \delta_n \\ \delta_{s2} \\ \delta_{s1} \end{Bmatrix} = \mathbf{K}\boldsymbol{\delta} \tag{2}$$

The off-diagonal terms in the elasticity matrix $\mathbf{K}$ are set to zero, which provides an uncoupled behavior between the traction vector and separation vector. The initial stiffness of non-thickness CIEs does not represent a physically measurable quantity and is treated as a penalty parameter. Ideally, the initial stiffness of CIEs should be infinite so that they do not affect the global compliance of the model before the damage initiation. However, a finite value must be used in the context of combined FDEM. Such an artificial stiffness is represented by the normal and shear penalty values, k_n, and k_s. For practical purposes, the cohesive contribution to the overall model compliance can be largely limited by adopting a very high penalty values [17,32]. However, larger values of the interface stiffness may cause numerical problems, such as spurious traction oscillations of the tractions [33]. Thus the interface stiffness should be large enough not to alter the overall stiffness of the model but small enough to reduce the risk of numerical problems. Different guidelines have been proposed for selecting the stiffness of CIEs in composite materials based on experience [34–36]. Following the approach initially proposed by Song et al. [37] and Turon et al. [38], and later adopted by Lens et al. [39], the stiffness of non-thickness CIEs is determined in terms of the elastic modulus and the length of the region surrounding the CIEs. The effective Young's modulus of a system consisting of solid elements bonded with non-thickness CIEs is estimated as [37–39]:

$$E_{\text{eff}} = E\left(\frac{1}{1 + E/(k_n l_e)}\right) \tag{3}$$

where E is the Young's modulus of the bulk material, l_e is a characteristic length scale, which is taken as the average mesh size of all bulk finite elements, and k_n is the initial stiffness of the interface in the normal direction. The effective elastic properties of the system will not be affected by the CIEs whenever the inequality $E << k_n l_e$ is being satisfied, i.e.:

$$k_n = \frac{\alpha E}{l_e} \tag{4}$$

where α is a parameter much larger than 1.

Furthermore, similar expression can be derived for shear stiffness:

$$k_s = \frac{\alpha G}{l_e} \tag{5}$$

where G is the shear modulus of the bulk material.

The use of Eqs. (4) and (5) is preferable to guidelines presented in previous work because it results from mechanical considerations, and it provides a sufficient stiffness while avoiding spurious oscillations caused by an excessively stiff interface.

Failure of the traction-separation response is defined within the general framework used for quasi-brittle materials, which consists of two ingredients: a damage initial criterion and a damage evolution law. The initial response of the cohesive element is assumed to be linear as discussed above. Depending on the local tractions of a CIE, interface damage can occur in mode I, model II, and in mixed-mode I/II. A mode I damage initiates when the normal traction, t_n, reaches the tensile strength of the material, f_t. As the damage processes, the normal traction, t_n, is assumed to gradually decrease to zero and a traction-free surface is then created. The mode II damage is initiated when the tangential traction, $t_{shear} = \sqrt{t_{s1}^2 + t_{s2}^2}$, reaches the shear strength of the material, f_s. The tensile strength, f_t, is assumed to be a constant, while the shear strength, f_s, is defined by the Mohr-Coulomb criterion with a tension cut-off:

$$f_s = \begin{cases} c - t_n \tan \varphi_i & \text{if } t_n < f_t \\ c - f_t \tan \varphi_i & \text{if } t_n \geq f_t \end{cases} \tag{6}$$

where c is the internal cohesion, φ_i is the material internal friction angle. Note here positive normal tractions are considered to represent tension, whereas negative normal stress components indicate compression.

The use of Mohr-Coulomb criterion in the formulation of CZM is not particularly new, see for instance Camacho and Ortiz [40] and Lens et al. [39]. Upon undergoing the shear strength, f_s, the tangential traction is gradually reduced to a residual value, f_r, which corresponds to a purely frictional resistance:

$$f_r = -t_n \tan \varphi_f \tag{7}$$

where φ_f is the fracture friction angle after the breakage of the embedded CIE.

For mix-mode loading, interface damage is assumed to initiate when a quadratic interaction function involving the tensile strength, f_t, and shear strength, f_s, reaches a value of one, as defined in the expression below:

$$\left[\frac{\langle t_n \rangle}{f_t} \right]^2 + \left[\frac{t_{shear}}{f_s} \right]^2 \geq 1 \tag{8}$$

where $\langle \rangle$ is the Macaulay bracket considering that compressive normal traction do not affect damage onset.

From an energetic point of view, as there are stresses to be overcome in propagating a crack, energy is dissipated during the fracturing process. Under single-mode loading, the area under the traction-separation curves in Fig. 2a, b represents the critical energy release rate in the corresponding fracture mode. Under mixed-mode loading, the total critical energy release rate, G_C, required to fully break a unit crack surface area, is normally established in terms of an interaction between the energy release rates and their critical values. The most widely used criterion to predict damage evolution under mixed-mode loading is the power law criterion:

$$\left(\frac{G_I}{G_{IC}} \right)^\beta + \left(\frac{G_{II}}{G_{IIC}} \right)^\beta = 1 \tag{9}$$

where G_{IC} and G_{IIC} are critical energy release rate in pure tension and shearing modes, respectively. β is a material parameter derived from mixed-mode tests and will generally assume values between 1 and 2. For $\beta = 1$ and $\beta = 2$ the linear criterion and the quadratic criterion are recovered, respectively.

Knowing G_{IC} and G_{IIC} for pure mode I and mode II, and the mode ratio G_I/G_{II}, we may then use Eq. (9) to obtain a G_C such that, at propagation:

$$G_C = G_I + G_{II} \tag{10}$$

For linear damage evolution, the damage variable, D, is determined using the following expression:

$$D = \frac{\delta_m^f \left(\delta_m^{max} - \delta_m^0 \right)}{\delta_m^{max} (\delta_m^f - \delta_m^0)} \tag{11}$$
$$\delta_m^f = 2G_C / t_{eff}^0$$

where δ_m^{max} refers to the maximum value of the effective relative displacement attained during the loading history. δ_m^0 and δ_m^f are the effective relative displacements at damage initiation and complete failure, respectively. t_{eff}^0 is the effective traction at damage initiation. The effective displacement, δ_m, and effective traction, t_{eff}, are defined as follows:

$$\delta_m = \sqrt{\langle \delta_n \rangle^2 + \delta_{shear}^2} = \sqrt{\langle \delta_n \rangle^2 + \delta_{s1}^2 + \delta_{s2}^2}$$
$$t_{eff} = \sqrt{\langle t_n \rangle^2 + t_{shear}^2} = \sqrt{\langle t_n \rangle^2 + t_{s1}^2 + t_{s2}^2} \tag{12}$$

where $\langle \rangle$ is the Macaulay bracket.

3 Validation of particle breakage modeling using combined FDEM

Single particle crushing tests were first performed on spherical grain to validate the particle breakage modeling in the context of the combined FDEM. The spherical morphology eliminates the complications caused by the irregular shapes of real particles. As shown in the schematic diagram of crushing test in Fig. 3, a rock grain with diameter of 60 mm was placed between two rigid platens, then vertically lowering the upper one to force the grain to break, while the bottom plate was totally fixed. The grain is meshed by quadratic tetrahedral elements and non-thickness CIEs, and the average mesh size is approximately 10 mm. A total number of 647 tetrahedral elements and 4723 CIEs are generated. The friction coefficient between the grain and rigid plates is set to 0.1. A time step $\Delta t = 1 \times 10^{-7}$s is used in the numerical simulations. The tensile strengths of the CIEs are randomly assigned based on a lognormal distribution, with other parameters, i.e., cohesion, friction angle of intact material, and fracture energies are given in Table 1. For simplicity, the internal friction angle, φ_i, and ratio of uniaxial compressive strength to tensile strength, f_c/f_t, are set to 50° and 15, respectively. The cohesion strength is then calculated as $c = 15 f_t(1 - \sin \varphi_i)/(2 \cos \varphi_i)$. The parameters summarized in Table 1 are assumed to represent the medium crushability particle.

Extensive Monte Carlo simulations with different random thresholds for the CIEs were conducted to investigate the statistical characteristics of the fracture strength of grains. It has been proved that at least 30 tests are required to give a statistical representation of the average strength and the distribution of strengths. The reaction force on the top plate together with the broken CIEs in every 0.04 mm of loading displacement are recorded and illustrated in Fig. 3a. Before reaching the peak force, the grain deforms linearly and only a small number of CIEs has been broken. A single dominant peak force of approximately 12.4 kN appears at a displacement of 0.16 mm, followed by a sharp drop in the load-bearing capability. Before this dominant peak, the curve has an overall steep slope with slight fluctuation due to a series of minor perturbations caused by local CIE breakages. After reaching

Fig. 3 Single particle crushing tests results: **a** simulated force-displacement curve and histogram of broken CIEs in every 0.04 mm of loading displacement; **b** fracture process of particle in crushing test arranged in time sequence
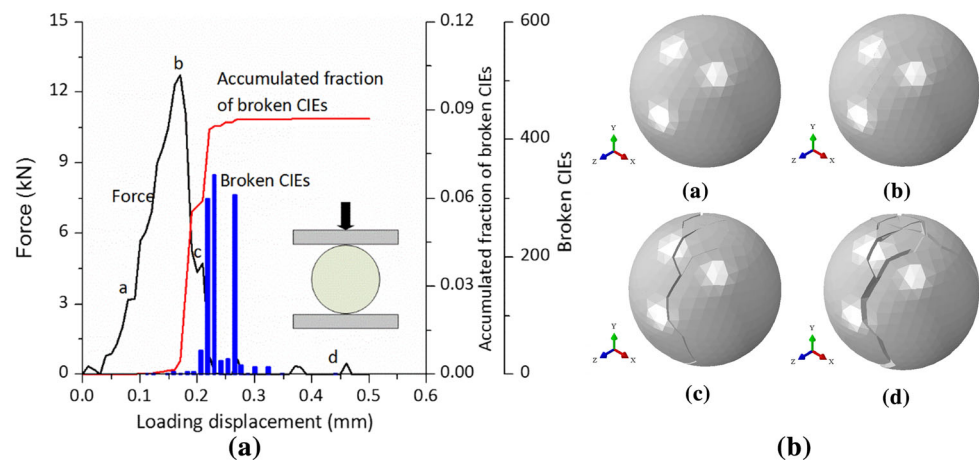
Table 1 Input parameters used in combined FDEM modeling

	Parameter	Value
Bulk elements	Mass density, ρ (kg/m^3)	2700
	Young's modulus, E (GPa)	40
	Poisson's ratio, υ	0.2
Cohesive elements	Tensile strength of CIE, f_t (MPa)	Lognormal distribution with mean value of 25 MPa and variation coefficient of 0.5
	Friction angle of intact material, φ_i (°)	50°
	Friction angle of fractures, φ_f (°)	26.56°
	Cohesion of CIE, c (MPa)	$c = 15 f_t(1 - \sin \varphi_i)/(2 \cos \varphi_i)$
	Mode-I fracture energy, G_I (N/m)	190
	Mode-II fracture energy, G_{II} (N/m)	950
Contact law	Inter-particle sliding friction, μ	0.5

the peak, more cracks formed the gradually connect to each other, leading to the final splitting of the particle. Finally, the grain is seen to split into three major pieces and some debris.

Figure 3b shows the progressive fracture pattern of the grain under compression. The letters in the figure indicate the different loading stages, which are labeled in Fig. 3a. There is no CIE breakage in the linear elastic stage and few CIE breaks as an indication of crack initiation. Damage initiates from the contact zone between the grain and top platen, in where the circumferential stress field is tensile. Cracks initiate from the contact point between the grain and top platen, and then run through during the softening stage, roughly parallel to the direction of loading to form meridional planes. For all configurations, a sharp transition from the damage to the fragmentation region is observed. The fracture pattern is very similar to the single particle loading tests of spherical particles [41,42], but also the breakage of spherical particles at impact loading [43,44]. Although the mechanical responses of a single particle at static and impact loading are different, the overall fracture patterns are similar. We show that this primary fracture mechanism is very robust with respect to the internal structure of the grain. The validity of the numerical simulation of single particle crushing test can be demonstrated quantitatively by comparing the simulated behavior with the experimental results of platen compression tests on single quartz by Nakata et al. [45].

It has been theoretically and experimentally verified that the grain tensile strength follow a Weibull distribution well [46]. For a given rock grain of average size d loaded diametrically, an induced characteristic strength σ is defined as the diametral force at failure F divided by the square of the particle diameter, which may be taken to be the distance between the platens at failure:

$$\sigma = \frac{F}{d^2} \tag{13}$$

Based on the Weibull model, the cumulative probability P_s that a grain of size d survives a tensile stress σ can be described as:

$$P_s = \exp\left[-\left(\frac{d}{d_0}\right)\left(\frac{\sigma}{\sigma_0}\right)^m \right] \tag{14}$$

where d_0 is a reference size and σ_0 is the characteristic stress for a grain of size d_0 to give a survival probability of 37%, m is the Weibull modulus which describes the variability in the tensile strength of different grains.

For a finite number of tested grains, the survival probability P_s is calculated using the mean rank position:

$$P_s = 1 - \frac{i}{N+1} \tag{15}$$

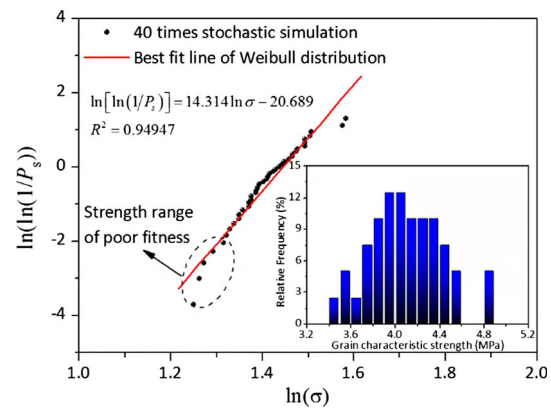where N is the total number of grains and i is the rank of the grain sorted in an ascending order.

Fig. 4 Comparison of simulation data with Weibull's equation

By rewriting Eq. (14) with $d = d_0$, a linear relationship can be obtained:

$$\ln\left[\ln\left(1/P_s\right)\right] = m \ln \sigma - m \ln \sigma_0 \tag{16}$$

Taking $\ln \sigma$ and $\ln\left[\ln\left(1/P_s\right)\right]$ as the x- and y-axis, which is a plot of $\ln\left[\ln\left(1/P_s\right)\right]$ against $\ln \sigma$, the Weibull modulus m is the slope of the best fit line, and the value of σ_0 is the value of σ when $\ln\left[\ln\left(1/P_s\right)\right] = 0$. The simulated data points and the corresponding fitting curves according to Eq. (16) for the spherical grains are plotted in Fig. 4. The data points satisfy the Weibull distribution well, except at lower strength ranges the data deviates from the Weibull best fit line. The Kolmogorov Smirnov goodness of fit test is performed and the returned vale of 0 indicates a failure to reject the Weibull hypothesis at the 0.05 significance level. This result indicate that, with the assumption of the strength of CIEs obey lognormal distribution, the behavior of the grains is approximately Weibullian. This is in excellent agreement with experimental results presented in [42,47], and DEM modeling results presented in [11,48].

4 Triaxial compression tests of breakable granular materials

4.1 Numerical sample preparation

The polydisperse assembly representing the granular materials consists of irregular shaped polyhedral particles. Each particle is randomly generated within an ellipsoid by a specially designed and efficient algorithm [23]. To achieve a balance between the sample representativity and affordable CPU time, the equivalent particle diameter ranges from 9 mm (d_{min}) to 27 mm (d_{max}) with a Rosin-Rammler distribution, giving a mean grain diameter (d_{50}) of 18 mm (as shown in Fig. 5). The equivalent particle diameter is defined as the diameter of a sphere with equal volume of the irregular
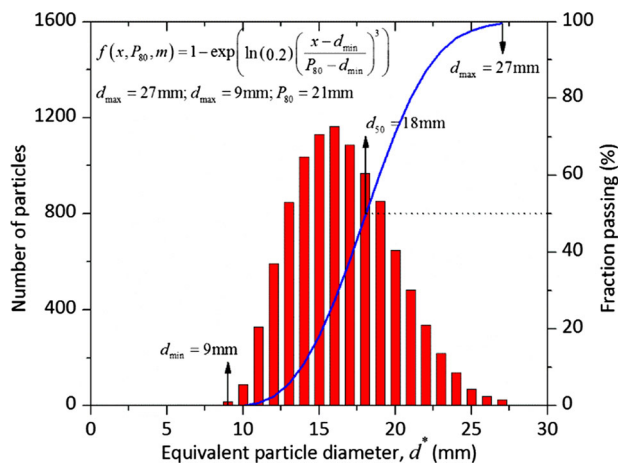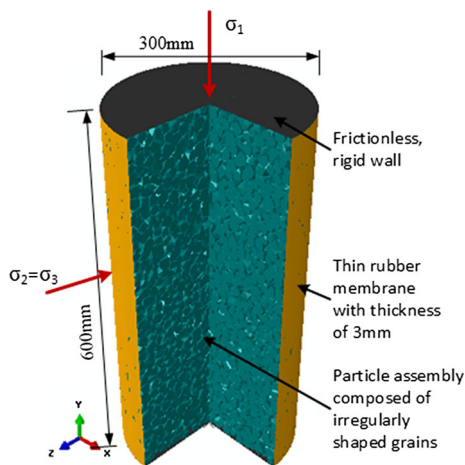
Fig. 5 Particle size distribution

Fig. 6 Schematic diagram of triaxial test and numerical sample

shaped particle. Firstly, for guaranteeing no initial contact overclosure, a loose assembly of 10,063 polyhedral particles was generated using random deposition. Following the geometric processing, the assembly was compacted uniaxially insider a cylinder until the desired sample height was reached, which is similar to the tamping method in laboratory test. During the sample preparation, the inter-particle friction coefficient was set to zero to obtain a relatively dense packing, and the particle breakage was also disabled. The final configuration of the numerical sample shown in Fig. 6 has a void ratio of 0.5625 corresponding to a relativity dense granular packing. The average mesh size is approximately 4 mm. On average, each particle is discretized into 350 quadratic tetrahedral elements and 2000 CIEs to reproduce a realistic fracture pattern.

4.2 Triaxial test set-up

The virtual triaxial compression test set-up is illustrated in Fig. 6. The numerical sample with diameter of 300 mm and

height of 600 mm was placed between the top and bottom rigid platens and externally reinforced by a thin and flexible membrane. In the numerical triaxial testing of granular materials, special-purpose elements are necessary to model the rubber membrane used to provide the confinement of the sample. Such membrane has been modeled with chains of circular or spherical particles in prior discrete element simulations [49,50]. In combined FDEM modeling, the rubber membrane is modeled with the deformable membrane elements with Ogden hyperelastic material model that can transmit in-plane force only and has no bending stiffness, which is allowed to deform flexibly to mimic the laboratory sample deformation. The hyperelastic model is based on the assumption of isotropic behavior throughout the deformation history. Hence, the hyperelastic materials are described in terms of a strain energy potential, which defines the strain energy stored in the material per unit of reference volume as a function of the strain at that point in the material. There are several forms of strain energy potentials available to model approximately incompressible isotropic rubberlike materials, such as the Ogden form. The Ogden hyperelastic material model and the multiple experimental results used to fit the model parameters can be found in ABAQUS user's manual [28].

The numerical triaxial test was performed using the following protocol. The numerical sample was initially compacted hydrostatically to a prescribed confining pressure. Then, the sample was sheared by displacing the top platen in a downward direction at constant velocity, while the confining pressure acting on the exterior surface of the membrane was kept constant, and the bottom platen was fixed. The triaxial shearing continued until the axial strain reached around 16 %. The loading velocity is slow enough to ensure the sample is sheared under quasi-static condition. The simulations were performed using 24 Intel Xeon 2.4 GHz processors and 16 GB DDR3 1600 MHz RAM memory at the Water Resources and Hydropower High Performance Computing Center. The CPU time takes about 37 h per simulation.

4.3 Choosing input parameters

A typical combined FDEM simulation requires various input parameters. The selection of these parameters is very important to reflect accurately a real problem. As described above, the crushability of the particles is represented by the CIE strength and characterized by the Mohr-Coulomb criterion with tension cut-off which consists of three parameters, the uniaxial tension strength f_t, internal friction angle, φ_i, and cohesion strength, c, respectively. It should be noted that φ_i and c are used to quantify the strength of CIE but not the granular materials itself. The parameters listed in Table 1 are used in this qualitative study.

5 Simulation results of numerical triaxial tests

5.1 Comparisons of breakable and unbreakable granular materials

Under conventional triaxial conditions with vertical compression, we have $\sigma_1 \geq \sigma_2 = \sigma_3$, where σ_1, σ_2, and σ_3 are the principal stresses. The mean and deviator stresses are expressed as $p = (\sigma_1 + 2\sigma_3)/3$ and $q = \sigma_1 - \sigma_3$, respectively. An area correction and membrane correction are applied to all numerical triaxial tests. The cross sectional area of the numerical sample is corrected during consolidation and shearing phases assuming that the sample deforms as a right circular cylinder. It is generally well established in the literature that the membrane provides resistance to the applied loads and that it is necessary to correct for its contribution. A positive value of volumetric strain indicates compression while a negative value indicates dilation.

Comparative numerical triaxial tests were conducted on breakable and unbreakable granular assemblies, respectively. At the very beginning, both granular assemblies have identical configuration, except that non-thickness CIEs are embedded into the finite element mesh of the breakable one, while particles in the unbreakable one can deform only. Figure 7 shows the deformations of breakable granular assembly during the shearing process at confining pressure of 0.8 MPa, the color of particles indicates the magnitude of displacement. Bulging is shown in all of the subplots, similar to that observed by laboratory test. Due to the particle breakage, the bulging of breakable granular assembly is milder than the unbreakable one. The three-dimensional view of particle breakages in a dense granular assembly is difficulty to capture, so a cut plane perpendicular to the y-direction and passing through the center of the granular assembly is made to show displacement and particle breakages in this plane(as shown in Fig. 8a). Compared with the breakable assembly in Fig. 8c, a relatively clear "X" type shear band is formed in the unbreakable assembly in Fig. 8b, where the lateral membrane boundaries are seen to deform severely to form local "wraps" around the ends of the shear band, and similar observations were made by pervious DEM investigations [11]. This is a clear indication of strong dilation associated with strain localization, which is facilitated by the flexible lateral boundaries. However, this phenomenon is much reduced or completely absent in the medium to high crushability
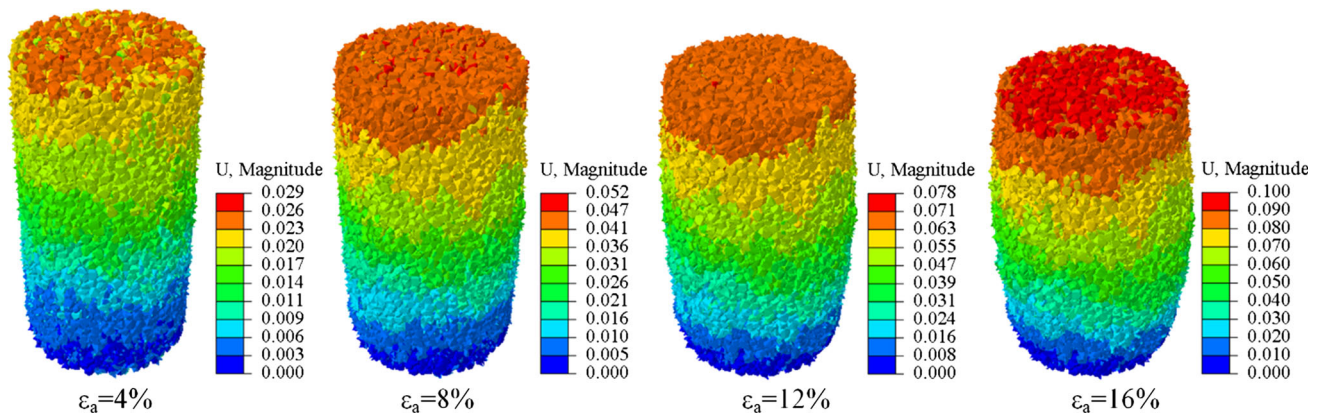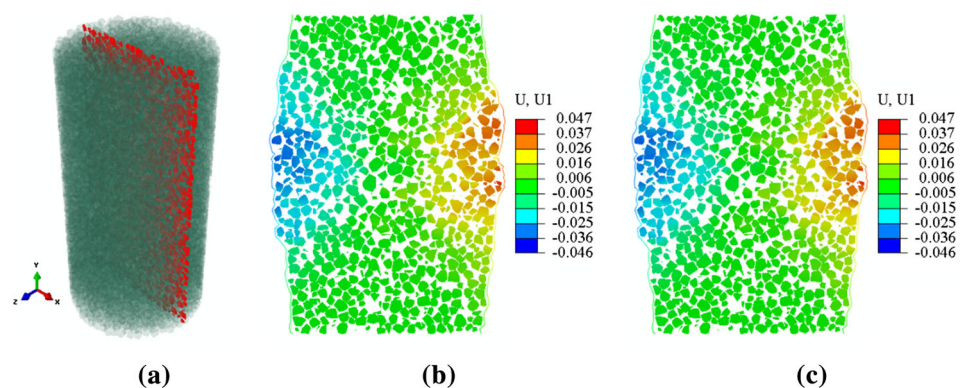

Fig. 7 Deformation of breakable granular assembly during the shearing process at confining pressure of 0.8 MPa (units: m)

Fig. 8 Lateral displacement contour and particle breakage in this plane for both assemblies at the end of sharing: **a** cut plane; **b** unbreakable assembly; **c** breakable assembly (same color legend is used for two assemblies. Units: m
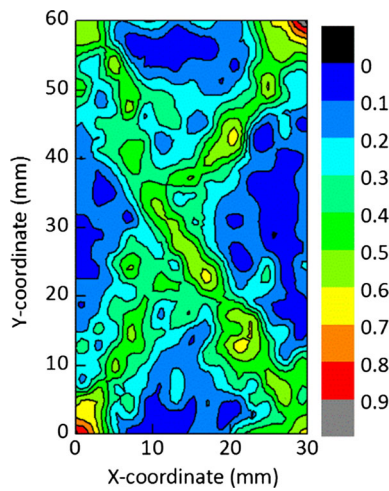
Fig. 9 Contour plot of broken density in the cut plane at the end of shearing

Fig. 10 Simulation results for two assemblies at confining pressure of 0.8 MPa

granular assemblies. The massive particle breakage becomes dominant so that large voids cannot be fully developed. Shear banding and volumetric compaction depict the two failure modes of a dense granular assembly, however, the more typical situation is the combination and competition of the two failure modes, especially in the medium crushability assemblies [11]. The particle breakage is moderate in the early stage of the shearing but interestingly develops into a distribution that generally falls within the major shear band at the end the shearing (Fig. 8c). This phenomenon can be more clearly demonstrated by the spatial distribution of broken density, which is also referred to as the fraction of broken CIEs. As shown in Fig. 9, the particle breakages mainly occur in the region of shear band. It is readily comprehensible because the strong contact force chains mainly concentrated within the shear band to drive the volumetric dilation, and particle breakage mainly occurs in this region is a natural result.

Figure 10 shows the macroscopic responses of two granular assemblies in terms of the deviator stress and volumetric strain versus axial strain. The figure shows qualitatively that the simulated stress–strain–dilation responses obtained for both assemblies are typical of those observed in laboratory tests. The initial tangential modulus, secant modulus, and peak shear stress are much higher for the unbreakable assembly, which exhibits an obvious peak at an axial strain of approximately 3.9 %, followed by a strain softening behavior. Furthermore, strong dilation is preceded by an initial slight compression followed by a significant volume expansion at large strains. Because of the extra energy required for the particles to dilate against the confining pressure, a dilative assembly has greater strength than a contractive assembly. Meanwhile, the dilation drives the particle assembly to move from a lower potential-energy state to a higher
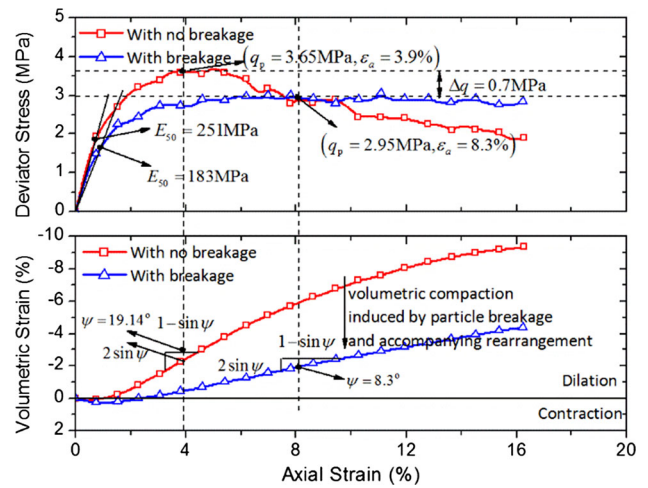
potential-energy state, causing the microstructure to become more unstable and ultimately decreasing the friction angle to residual state. In contrast, relatively slight volumetric expansion takes place in the granular assemblies with medium degree of crushability, and continuous volumetric compression takes places in the high crushability assemblies. This behavior is clearly a result of excessive particle breakage, which has an opposing effect on the dilative mechanism and suppresses the mobilization of the assembly dilation. As depicted in Fig. 10, where an overall dilatant behavior associated with slight post-peak softening is observed to dominant the medium crushability assembly, although a certain amount of particle breakages also take place during shearing.

The shear dilatancy behavior of the modeled granular materials is characterized in terms of the relationship between the stress ratio q/p and incremental strain ratio $-d\varepsilon_v/d\varepsilon_d$, where ε_v and ε_d are volumetric and deviator strains, respectively. It should be noted that the incremental strains $d\varepsilon_v$ and $d\varepsilon_d$ consist of both the elastic and plastic components. Figure 11 shows the relations between the stress ratio and incremental strain ratio for breakable and unbreakable granular assemblies at confining pressure of 0.8 MPa. The simulated results and observed trend for two assemblies can be fairly well fitted by linear functions, which indicate that the stress dilatancy behavior can be described by Modified Roscoe's dilatancy model [51]. At lower stress ratio ranges, the scatters deviate from the best fit line. This may be due to the presence of elastic strains, whose proportions are considerable to the plastic strains at low stress ratios. Figure 11 also illustrates that the fitting lines, which describe the observed trend from the simulated results, vary with the crushability of the granular assembly. The slope of the fitting line for breakable assembly is much stiffer than the unbreakable assembly. M is defined as the stress ratio corresponding to
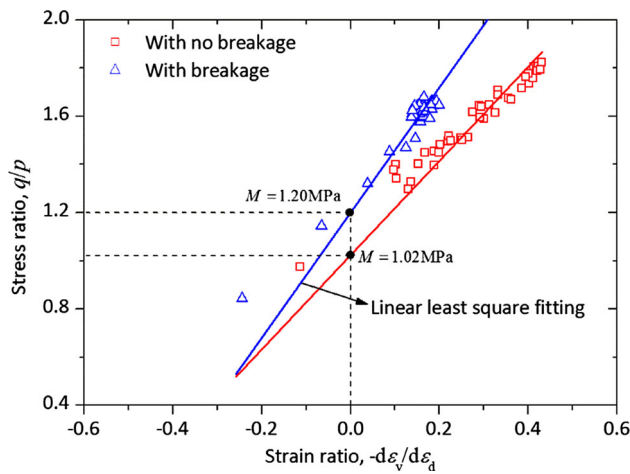
Fig. 11 Stress dilatancy behavior of two granular assemblies at confining pressure of 0.8 MPa

zero dilatancy, which is also termed as the slope of phase transformation line or characteristic line. The value of M is 1.20 and 1.02 MPa for breakable and unbreakable assembly, respectively.

5.2 Influence of confining pressure on the breakable granular materials

Four levels of confining pressures, 0.4, 0.8, 1.2 and 1.6 MPa were considered. The figure legend text indicates different confining pressures. Notwithstanding the discrepancies between macroscopic behavior observed in laboratory and numerical experiment, the numerical simulation can clearly capture the typical response of breakable granular materials (as shown in Fig. 12). The difference between the experimen-

tal and numerical responses lies primarily in the volumetric behavior, i.e., granular materials in laboratory tests show greater tendency of shear contraction due to their wide range of particle sizes and intensive particle breakage [23]. It can be seen that the initial tangential modulus, secant modulus, and peak deviator stress increase with increasing confining pressure. There is a tendency in stress–strain curves to reach a peak deviator stress followed by subsequent strain-softening at lower confining pressures. At higher confining pressures, strain-softening changes into strain-hardening type of behavior without a sharp peak in the deviator stress–strain curves. The variation of volumetric strain with axial strain curves describes an initial contractive behavior regardless of the magnitude of confining pressure, at lower confining pressures the initial volumetric compression is followed by subsequent volumetric dilation, while dilation is suppressed and only volumetric compression is measured at higher confining pressures. This type of behavior is characteristic of medium crushability granular materials with fairly dense initial packing [10,11,23].

The macroscopic responses analyzed previously are clearly a result of excessive particle breakage demonstrated by the evolutions of the accumulated fraction of broken CIEs with axial strain under different confining pressures (as shown in Fig. 13). The particle breakage has a negligible effect on the mechanical behavior of granular materials at a low stress level. In the case of high stress level, this effect is significant and cannot be ignored. Figure 14 shows the evolutions of the frequency of broken CIEs, accumulated fraction of broken CIEs, and deviator stress during the shearing process with the confining pressure of 0.8 MPa. Each red bar indicates the number of broken CIEs happened in every 0.4 % of axial strain, which represents the frequency of parti-
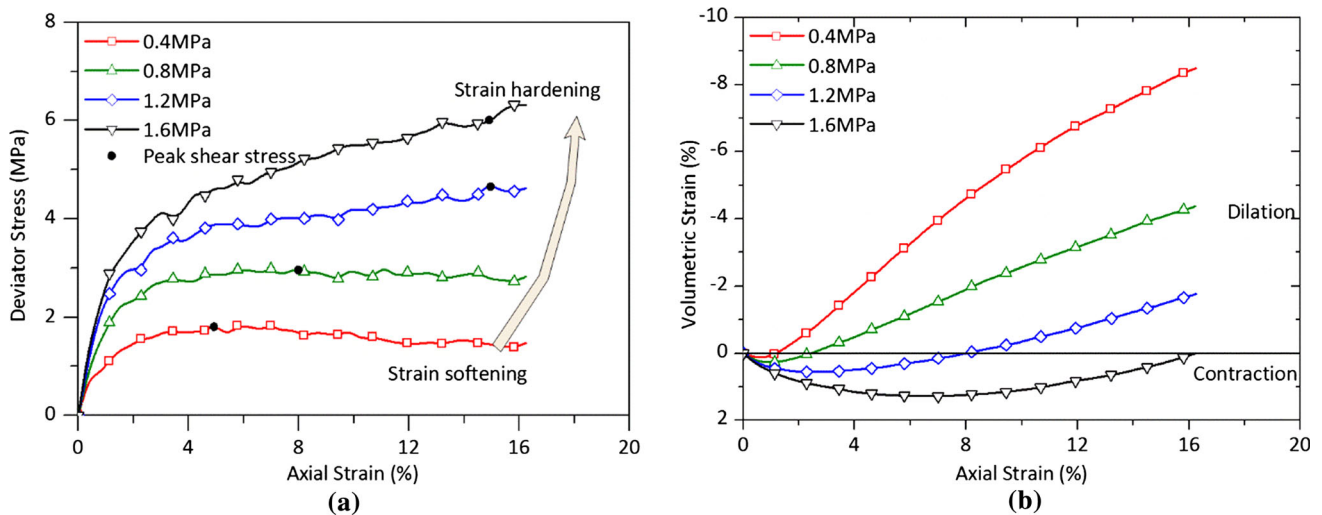

Fig. 12 Macroscopic responses of breakable granular assembly under different confining pressures: **a** deviator stress versus axial strain; **b** volumetric strain versus axial strain
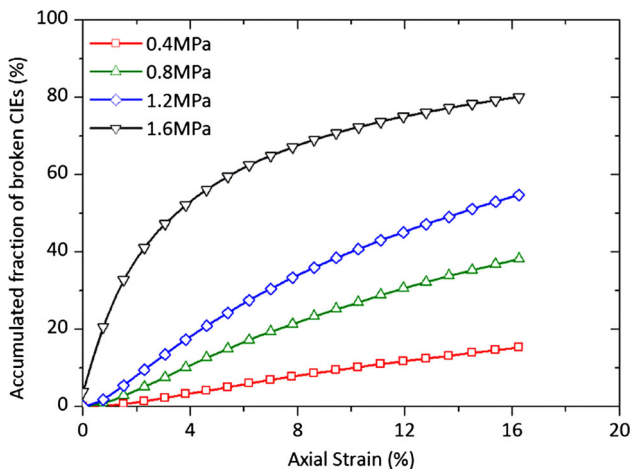
Fig. 13 Evolutions of accumulated fraction of broken CIEs with axial strain under different confining pressure
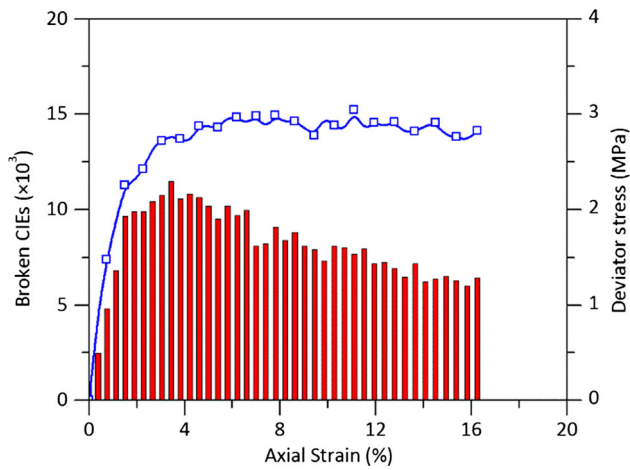

Fig. 15 Curves of dilatancy index versus axial strain at different confining pressures

Fig. 14 Correlation between the frequency of broken CIEs and deviator stress at confining pressure of 0.8 MPa
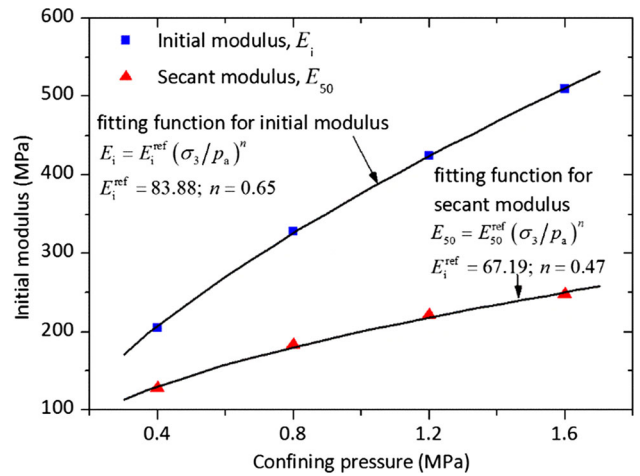
Fig. 16 Variations of the deformation characteristics of breakable assembly with confining pressure

cle breakage. The frequency of broken CIEs rapidly increases at a small strain level and experiences a reduction after the peak value.

To further investigate the effect of confining pressure on the dilatancy of the granular materials, the relationships between dilatancy index and axial strain for different confining pressure are presented in Fig. 15, where dilatancy index is defined as $-d\varepsilon_v/d\varepsilon_a$. Note that the trend of dilatancy index for breakable assembly is quite different under different confining pressures. The dilatancy index decreases with the increase of confining pressure. The evolutions of dilatancy index with axial strain for unbreakable assembly are aligned in a narrow band, which indicates that the dilatancy behavior of unbreakable granular materials is independent of the confining pressure. The previous DEM study also confirmed that the dilatancy behavior is rather independent of extremely low confining pressures [52]. This is because very few particle breakages occur when the stress level is extremely low.
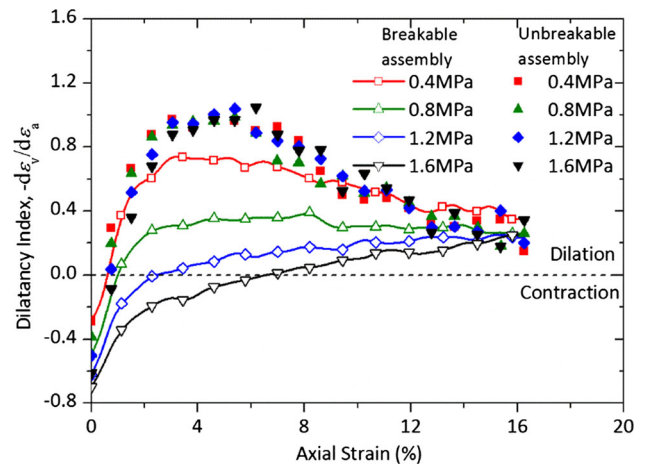
The macroscopic behavior derived from the numerical triaxial tests can be quantified by initial elastic modulus, secant modulus, peak friction angle, and dilatancy angle. The initial elastic modulus E_i indicates the deformation behavior of granular materials, which corresponds to the initial slope of the stress–strain curve. The axial strain is constrained within 0.1 % for the initial slope of the stress–strain curve, where the deformation is supposed to be elastic. As shown in Fig. 16, the initial elastic modulus E_i of breakable granular materials at a given void ratio increases with an increase in the confining pressure. In the constitutive modeling of sands, soils, etc., the secant modulus E_{50} is more commonly used, which is defined as the secant modulus at 50 % of the peak deviator stress. Similar to the initial elastic modulus, the secant modulus E_{50} shows a gradual increase with increasing confining pressure. As demonstrated before, the extent of particle breakage increases with increasing stress level, which slows down the increasing trend of both the initial elastic modulus

and secant modulus. Both two moduli can be correlated with the confining pressure by a power function with different fitting parameters, where p_a is atmospheric pressure used for normalization.

The variations of peak friction angle φ_p and dilation angle ψ with confining pressure are shown in Fig. 17. For breakable granular assembly, an increase in the confining pressure would lead to a decrease in both the angle of shearing resistance and dilation angle. This relationship is attributed to two causes: An intense amount of particle breakage, and a decrease in dilation due to increased confinement under higher confining pressures. The relationships between peak friction angle and dilation angle with confining pressure can be described by exponential functions with different fitting parameters. Another observation is that the peak friction angle and dilation angle for unbreakable granular assembly
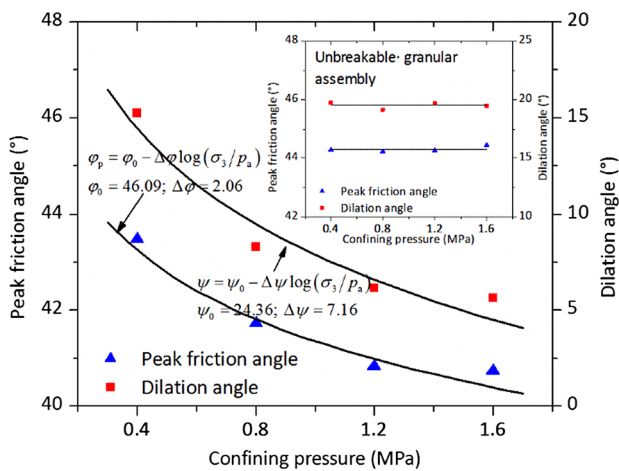
do not change over confining pressure (as shown in the inset of Fig. 17). The comparison leads to the important conclusion that the stress dependency of the peak friction angle and dilation angle of granular materials is primarily caused by particle breakage. It can be concluded that the variations of peak friction angle for breakable and unbreakable granular assemblies will converge to the same value at extremely low stress level, and so does the dilation angle, where particle breakage is largely absent.

5.3 Effect of particle crushability on the breakable granular materials

A group of numerical triaxial tests were carried out on an identical particle assembly but with varied CIE strength parameters to investigate the effect of particle crushability on the mechanical behavior of granular materials. The five levels of particle crushability considered are 8, 10, 15, 20 and 25 MPa, respectively, each denotes the mean value of CIE tensile strength. Numerical triaxial tests in this part were performed with the confining pressure of 0.8 MPa. As illustrated in Fig. 18a, the macroscopic response of assembly with lower particle crushability, i.e., higher particle strength, are characterized by obvious strain softening. The deviator stress decreases gradually with the increasing particle crushability, accompanied by an appreciable reduction of post-peak strain softening extending to large strains. The stress response is intrinsically related to the volumetric response shown in Fig. 18b. For assembly with low crushability, strong dilation is observed by an initial slight compaction followed by a significant volume expansion. Continuous volumetric compaction takes place in the assembly of a high degree of crushability. The above description can be explained by the
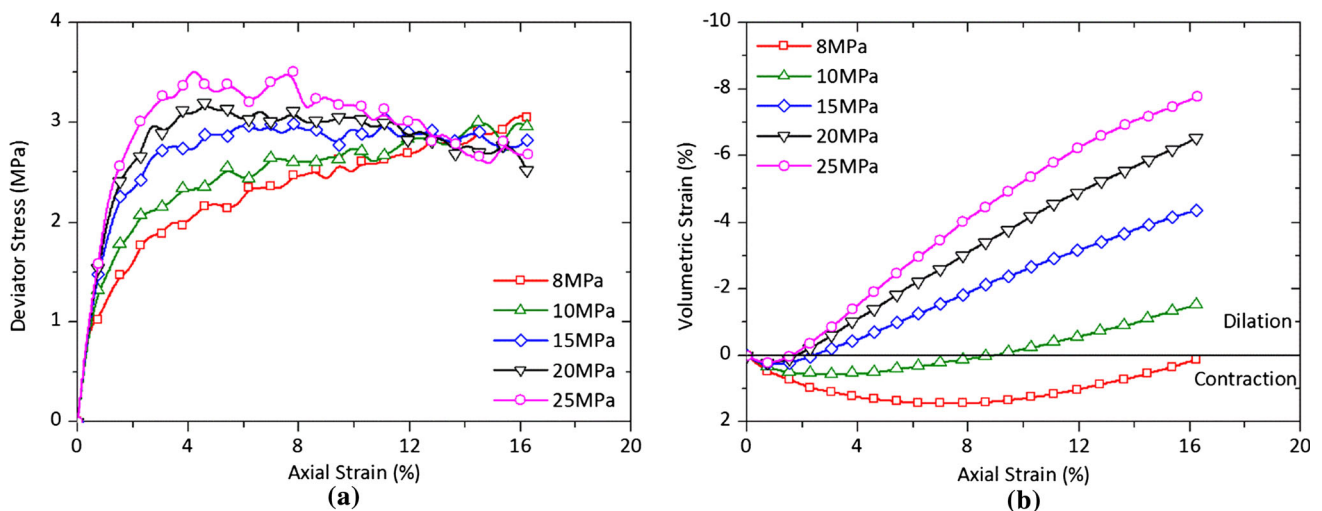

Fig. 17 Variations of peak friction angle and dilation angle of breakable assembly with confining pressure

Fig. 18 Macroscopic responses of breakable granular assembly under different particle crushability: **a** deviator stress versus axial strain; **b** volumetric strain versus axial strain
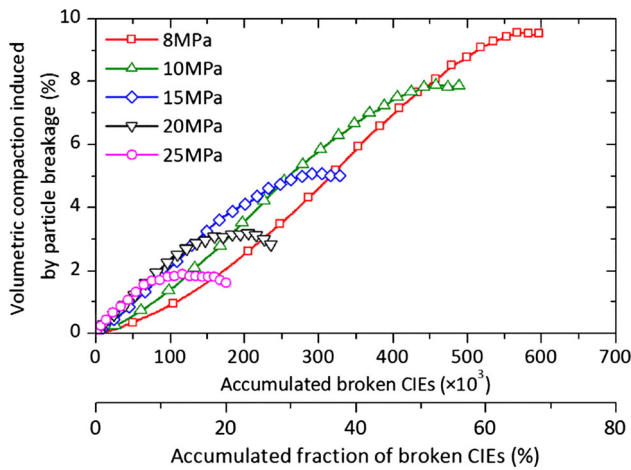
Fig. 19 Relations between net volumetric compaction and degree of crushing under different particle crushability

evolutions of accumulated fraction of broken CIEs with axial strain.

Figure 19 shows the net volumetric compaction induced by particle breakage as function of the degree of crushing. The net volumetric compaction is calculated as the volumetric strain of breakable granular assembly subtracts the volumetric strain of unbreakable strain. There is a positive relationship between them. However, in case of different particle strength or confining pressure, fully unified correlation does not exist between the net volumetric compaction and the degree of crushing. This is due to the volumetric compaction not only induced by particle breakage, but also the accompanying particle rearrangement. From the microscopic point of view, the difficulty in quantifying the effects of particle breakage on the macroscopic behavior stems mainly from two issues, namely the roles of particle breakage and the accompanying changes in fabric [11].

5.4 The energy dissipation in breakable granular materials

In the shearing of granular materials, there exists various kinds of energy, such as strain energy, kinetic energy, etc.. They could transform into each other, while some of them would dissipate if sliding or particle breakage occurs. In DEM modeling, the strain energy is stored at contact points upon particle deformation, while in combined FDEM modeling, the strain energy in stored in a particle due to deformation. In reality, the strain energy that is released when brittle materials fracture is converted into surface energy and acoustic energy. Kinetic energy is primarily caused by the translation and rotation of particles in the process of rearrangement and crushing. Due to the quasi-static nature of the simulation, kinetic energy will be negligible in comparison to friction dissipation energy and strain energy.

In this paper, the particles are defined as completely elastic collision, i.e., coefficient of restitution is 1 and damping coefficient is 0, so the energy dissipation caused by mutual collisions between particles is not considered. The two energy dissipation mechanisms are caused by frictional slippage and particle breakage, respectively. The stored strain energy will be lost when the CIE is broken. The friction dissipation energy is calculated by summing the slip work done at all contacts where inter-particle sliding occurs.

To investigate the evolution of work input and energy dissipation during the shearing process of breakable granular materials, the various energy terms in the incremental form were traced and analyzed. These energy terms include the work input at the boundary dW, strain energy dE_s, kinetic energy dE_k, friction dissipation energy dE_f, and energy loss due to particle breakage dE_d. The above decomposition is made to facilitate a convenient investigation into the particle scale work input and energy dissipation characteristic [7,53,54]. According to the first law of thermodynamics, the energy components satisfy:

$$dW = dE_s + dE_f + dE_k + dE_d \tag{17}$$

The last three terms can be combined to form plastic dissipation:

$$dE_p = dE_f + dE_k + dE_d \tag{18}$$

So we can rewrite Eq. (17) as $dW = dE_s + dE_p$. This superficially analogous to Cam-Clay plasticity theory.

Figure 20 shows the evolutions of four incremental energy components against the axial strain for granular assembly with medium crushability. The incremental strain was taken to be 0.08 %. It is clear that the profile of the incremental work input has an overall good agreement with the development
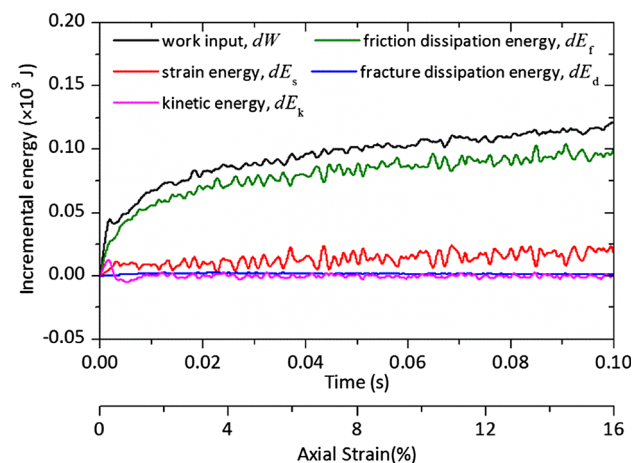

Fig. 20 Incremental energy components versus axial strain at confining pressure of 0.8 MPa
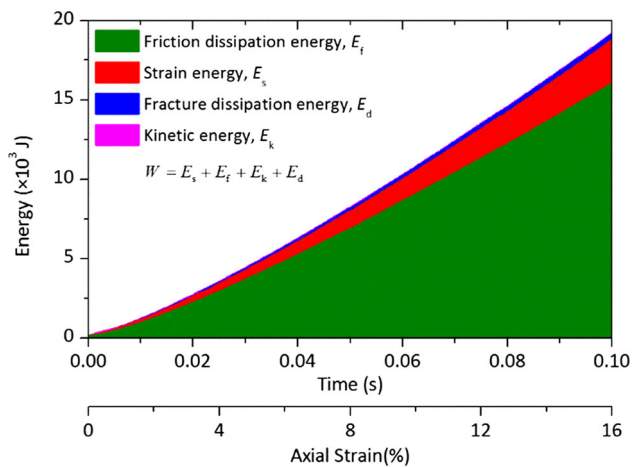
Fig. 21 Accumulated energy components versus axial strain at confining pressure of 0.8 MPa

of stress ratio with axial strain. In previous DEM modeling of granular materials [53,54], the incremental strain energy dE_s, except within the first few percentages of axial strain, essentially fluctuates around zero. However, in combined FDEM modeling, the incremental strain energy dE_s undergoes a very slow increase within the range of strain simulated. Despite this, the incremental plastic dissipation dE_p takes the majority of the incremental boundary work dW. This indicates that the granular materials quickly develops a fabric condition that can fully dissipate the external work through inter-particle friction and particle breakage, and has very little capability of storing any further strain energy. The amount of incremental fracture dissipation dE_d is much smaller than the incremental strain energy dE_s and incremental friction dissipation dE_f. The major effect of particle breakage, which itself only dissipates a small amount of the external work, is to promote the changes in fabric characteristics by creating additional degrees of freedom for inter-particle motion, largely prohibiting the strain energy accumulation and facilitating the friction dissipation. Similar conclusions were acquired by previous DEM studies [7,54]. The evolutions of different accumulated energy with axial strain are shown in Fig. 21. The friction dissipation contributes most to the external work, strain energy comes second, and followed by fracture dissipation. The kinetic energy remains almost zero throughout the shearing process.

6 Summary

The cohesive zone model is introduced into the combined FDEM to make it possible to simulate the particle breakage of granular materials. The validity of particle breakage modeling is guaranteed by a successful simulation of fracture behavior of single particles. The splitting behavior resembling that of a quartz particle is captured with higher

CIE strength and smaller variability. More importantly, the Weibull's statistical distribution, which essentially controls the particle fracture behavior, is shown to be reproduced by such a modeling approach.

A polyhedral particle generation algorithm is adopted to enable a closer approximation of the true particle shapes. Despite its convex nature, the polyhedral particles can reproduce the geometry dependent behaviors of granular materials, such as particle interlocking and resistance to rolling. A series of numerical triaxial tests were simulated under different confining pressure and particle crushability, which give a representative set of mechanical behavior of granular materials. The fairly dense packing of breakable granular materials would show distinct dilatancy and obvious peak shear stress, as well as post-peak softening behavior, if the particle crushability and confining pressure are relatively low. Meanwhile, continuous volumetric compaction and gradual strain hardening behavior in highly crushable granular materials subject to high confining pressure. In general, the simulation results are qualitatively in good agreement with the experimental observations, which indicate that the combined FDEM is predictive and can reproduce the typical mechanical behavior of breakable granular materials. The combined FDEM modeling also provides an opportunity for a quantitative study of the micro-structure of granular materials, which give us a further understanding of the mechanical behavior at the particle scale. Some studies demonstrated that there exists a competition between size effects and particle loading conditions. Small grains have less fracture probability following Weibull theory, meanwhile, they have less contact points and hence larger stress anisotropy. A statistical evaluation of the evolution of particle size distribution may help to find out which mechanism plays a leading role. However, we have not been able to exact the necessary information from simulation results to perform such statistical analysis.

The shear band is much reduced or completely absent in the medium to high crushability granular assemblies. The massive particle breakage becomes dominant so that large voids cannot be fully developed, which largely prevents the development of a shear band. Additionally, the particles in the shear band were more likely to break because the strong contact force chains mainly concentrated within the shear band to drive the volumetric dilation. The incremental plastic dissipation takes the majority of the incremental boundary work. This indicates that the granular materials quickly develops a fabric condition that can fully dissipate the external work through inter-particle friction and particle breakage. The major effect of particle breakage, which itself only dissipates a small amount of the external work, is to promote the changes in fabric characteristics by creating additional degrees of freedom for inter-particle motion, largely prohibiting the strain energy accumulation and facilitating the friction dissipation.

References

1. Hardin, B.O.: Crushing of soil particles. J. Geotech. Eng. **111**(10), 1177–1192 (1985)
2. Lade, P.V., Yamamuro, J.A., Bopp, P.A.: Significance of particle crushing in granular materials. J. Geotech. Eng. **122**(4), 309–316 (1996)
3. Coop, M.R., Sorensen, K.K., Freitas, T.B., et al.: Particle breakage during shearing of a carbonate sand. Géotechnique **54**(3), 157–163 (2004)
4. Xiao, Y., Liu, H., Chen, Y., et al.: Strength and deformation of rockfill material based on large-scale triaxial compression tests. II: influence of particle breakage. J. Geotech. Geoenviron. Eng. **140**(12), 04014071 (2014)
5. Robertson, D., Bolton, M.D.: DEM simulations of crushable grains and soils. In: Kishino, Y. (ed.) Powders and Grains, pp. 623–626. Balkema, Lisse (2001)
6. Cheng, Y.P., Nakata, Y., Bolton, M.D.: Discrete element simulation of crushable soil. Geotechnique **53**(7), 633–641 (2003)
7. Bolton, M.D., Nakata, Y., Cheng, Y.P.: Micro-and macro-mechanical behaviour of DEM crushable materials. Géotechnique **58**(6), 471–480 (2008)
8. Donohue, S., O'sullivan, C., Long, M.: Particle breakage during cyclic triaxial loading of a carbonate sand. Géotechnique **59**(5), 477–482 (2009)
9. Cil, M.B., Alshibli, K.A.: 3D assessment of fracture of sand particles using discrete element method. Geotech. Lett. **2**(3), 161–166 (2012)
10. Alaei, E., Mahboubi, A.: A discrete model for simulating shear strength and deformation behaviour of rockfill material, considering the particle breakage phenomenon. Granul Matter **14**(6), 707–717 (2012)
11. Wang, J., Yan, H.: On the role of particle breakage in the shear failure behavior of granular soils by DEM. Int. J. Numer. Anal. Methods Geomech. **37**(8), 832–854 (2013)
12. Lobo-Guerrero, S., Vallejo, L.E.: Discrete element method evaluation of granular crushing under direct shear test conditions. J. Geotech. Geoenviron. Eng. **131**(10), 1295–1300 (2005)
13. Brosh, T., Kalman, H., Levy, A.: Fragments spawning and interaction models for DEM breakage simulation. Granul. Matter **13**(6), 765–776 (2011)
14. de Bono, J.P., McDowell, G.R.: DEM of triaxial tests on crushable sand. Granul. Matter **16**(4), 551–562 (2014)
15. Zhou, W., Yang, L., Ma, G., et al.: Macro–micro responses of crushable granular materials in simulated true triaxial tests. Granul. Matter **17**(4), 497–509 (2015)
16. Munjiza, A., Owen, D.R.J., Bicanic, N.: A combined finite-discrete element method in transient dynamics of fracturing solids. Eng. Comput. **12**(2), 145–174 (1995)
17. Munjiza, A.: The Combined Finite-Discrete Element Method. Wiley, New York (2004)
18. Latham, J.P., Munjiza, A.: The modelling of particle systems with real shapes. Philos. Trans. R. Soc. Lond. Ser. Math. Phys. Eng. Sci. **362**, 1953–1972 (2004)
19. Mahabadi, O.K., Cottrell, B.E., Grasselli, G.: An example of realistic modelling of rock dynamics problems: FEM/DEM simulation of dynamic Brazilian test on Barre granite. Rock Mech. Rock Eng. **43**(6), 707–716 (2010)
20. Vyazmensky, A., Stead, D., Elmo, D., et al.: Numerical analysis of block caving-induced instability in large open pit slopes: a finite element/discrete element approach. Rock Mech. Rock Eng. **43**(1), 21–39 (2010)
21. Smoljanović, H., Živaljić, N., Nikolić, Ž.: A combined finite-discrete element analysis of dry stone masonry structures. Eng. Struct. **52**(7), 89–100 (2013)
22. Chang, X.L., Hu, C., Zhou, W., et al.: A combined continuous–discontinuous approach for failure process of quasi-brittle materials. Sci. China Technol. Sci. **57**(3), 550–559 (2014)
23. Ma, G., Zhou, W., Chang, X.L., et al.: Combined FEM/DEM modeling of triaxial compression tests for rockfills with polyhedral particles. Int. J. Geomech. **14**(4), 1–14 (2014)
24. Ma, G., Zhou, W., Chang, X.L.: Modeling the particle breakage of rockfill materials with the cohesive crack model. Comput. Geotech. **61**(9), 132–143 (2014)
25. Latham, J.P., Anastasaki, E., Xiang, J.: New modelling and analysis methods for concrete armour unit systems using FEMDEM. Coast. Eng. **77**(7), 151–166 (2013)
26. Guo, L., Latham, J.P., Xiang, J.: Numerical simulation of breakages of concrete armour units using a three-dimensional fracture model in the context of the combined finite-discrete element method. Comput. Struct. **146**, 117–142 (2015)
27. Latham, J.P., Munjiza, A., Garcia, X., et al.: Three-dimensional particle shape acquisition and use of shape library for DEM and FEM/DEM simulation. Miner. Eng. **21**(11), 797–805 (2008)
28. ABAQUS 6.10. ABAQUS Analysis User's Manual. Dassault Systèmes Simulia Corp, Providence (2010)
29. Xu, X.P., Needleman, A.: Numerical simulations of dynamic crack growth along an interface. Int. J. Fract. **74**(4), 289–324 (1995)
30. Chandra, N., Li, H., Shet, C., et al.: Some issues in the application of cohesive zone models for metal–ceramic interfaces. Int. J. Solids Struct. **39**(10), 2827–2855 (2002)
31. Alfano, G.: On the influence of the shape of the interface law on the application of cohesive-zone models. Compos. Sci. Technol. **66**(6), 723–730 (2006)
32. Lisjak, A., Liu, Q., Zhao, Q., et al.: Numerical simulation of acoustic emission in brittle rocks by two-dimensional finite-discrete element analysis. Geophys. J. Int. **195**(1), 423–443 (2013)
33. Day, R.A., Potts, D.M.: Zero thickness interface elements–numerical stability and application. Int. J. Numer. Anal. Methods Geomech. **18**(10), 689–708 (1994)
34. Zou, Z., Reid, S.R., Li, S., et al.: Modelling interlaminar and intralaminar damage in filament-wound pipes under quasi-static indentation. J. Compos. Mater. **36**(4), 477–499 (2002)
35. Camanho, P.P., Davila, C.G., De Moura, M.F.: Numerical simulation of mixed-mode progressive delamination in composite materials. J. Compos. Mater. **37**(16), 1415–1438 (2003)
36. Diehl, T.: On using a penalty-based cohesive-zone finite element approach, part I: elastic solution benchmarks. Int. J. Adhes. Adhes. **28**(4), 237–255 (2008)
37. Song, S.H., Paulino, G.H., Buttlar, W.G.: A bilinear cohesive zone model tailored for fracture of asphalt concrete considering viscoelastic bulk material. Engi. Fract. Mech. **73**(18), 2829–2848 (2006)
38. Turon, A., Davila, C.G., Camanho, P.P., et al.: An engineering solution for mesh size effects in the simulation of delamination using cohesive zone models. Eng. Fract. Mech. **74**(10), 1665–1682 (2007)
39. Lens, L.N., Bittencourt, E., d'Avila, V.M.R.: Constitutive models for cohesive zones in mixed-mode fracture of plain concrete. Eng. Fract. Mech. **76**(14), 2281–2297 (2009)
40. Camacho, G.T., Ortiz, M.: Computational modelling of impact damage in brittle materials. Int. J. Solids Struct. **33**(20), 2899–2938 (1996)

41. Cheshomi, A., Sheshde, E.A.: Determination of uniaxial compressive strength of microcrystalline limestone using single particles load test. J. Pet. Sci. Eng. **111**(11), 121–126 (2013)

42. Huang, J., Xu, S., Yi, H., et al.: Size effect on the compression breakage strengths of glass particles. Powder Technol. **268**(12), 86–94 (2014)

43. Carmona, H.A., Wittel, F.K., Kun, F., et al.: Fragmentation processes in impact of spheres. Phys. Rev. E **77**(5), 463–470 (2008)

44. Russell, A., Aman, S., Tomas, J.: Breakage probability of granules during repeated loading. Powder Technol. **269**(1), 541–547 (2015)

45. Nakata, A.F.L., Hyde, M., Hyodo, H.: A probabilistic approach to sand particle crushing in the triaxial test. Geotechnique **49**(5), 567–583 (1999)

46. McDowell, G.R., Amon, A.: The application of Weibull statistics to the fracture of soil particles. Soils Found. **40**(5), 133–141 (2000)

47. Lim, W.L., McDowell, G.R., Collop, A.C.: The application of Weibull statistics to the strength of railway ballast. Granul. Matter **6**(4), 229–237 (2004)

48. Ergenzinger, C., Seifried, R., Eberhard, P.: A discrete element model predicting the strength of ballast stones. Comput. Struct. **108**(10), 3–13 (2012)

49. Cui, L., O'sullivan, C., O'neill, S.: An analysis of the triaxial apparatus using a mixed boundary three-dimensional discrete element model. Geotechnique **57**(10), 831–844 (2007)

50. Wang, Y., Tonon, F.: Modeling triaxial test on intact rock using discrete element method with membrane boundary. J. Eng. Mech. **135**(9), 1029–1037 (2009)

51. Li, X.S., Dafalias, Y.F., Wang, Z.L.: State-dependant dilatancy in critical-state constitutive modelling of sand. Can. Geotech. J. **36**(4), 599–611 (1999)

52. Sayeed, M.A., Suzuki, K., Rahman, M.M., et al.: Strength and deformation characteristics of granular materials under extremely low to high confining pressures in triaxial compression. Int. J. Civil Environ. Eng. **11**(4), 1–6 (2011)

53. Bi, Z., Sun, Q., Jin, F., et al.: Numerical study on energy transformation in granular matter under biaxial compression. Granul. Matter **13**(4), 503–510 (2011)

54. Wang, J., Yan, H.: DEM analysis of energy dissipation in crushable soils. Soils Found. **52**(4), 644–657 (2012)